Received: 12 January 2025 | Accepted: 6 March 2026

DOI: 10.1002/vzj2.70098

Vadose Zone Journal

ORIGINAL ARTICLE

Assessment of soil slurry saturation and slurry infiltration in pig slurry storage ponds using electrical resistivity tomography

Ximena Capa-Camacho[1] | **Pedro Martínez-Pagán**[2] | **Ángel Faz**[1] | **Marco Vásconez-Maza**[3] | **Marcos A. Martínez-Segura**[2] | **Khadidja Delimi**[2] | **Oussama Jabrane**[4]

[1]Sustainable Use, Management and Reclamation of Soil and Water Research Group, Department of Agricultural Engineering, Universidad Politécnica de Cartagena, Cartagena, Spain

[2]Applied Near-Surface Geophysics Research Group, Departamento de Ingeniería Minera y Civil, Universidad Politécnica de Cartagena, Cartagena, Spain

[3]British Geological Survey, Keyworth, Nottinghamshire, UK

[4]Department of Earth Sciences, Mohammed First Oujda University, Oujda, Morocco

Correspondence
Oussama Jabrane, Department of Earth Sciences, Mohammed First Oujda University, Oujda, 60000, Morocco. Email: o.jabrane@ump.ac.ma.

Assigned to Associate Editor Behzad Ghanbarian.

Funding information
Fundación Séneca. Región de Murcia (Spain), Grant/Award Number: 21583/FPI/21

Abstract

Effective management of pig slurry in semi-arid settings is critical to protect soils and aquifers. This study integrates multi-profile electrical resistivity tomography (ERT) compiled into stitched 3D volumes with a calibration based on modified Archie's law derived from laboratory resistivity–moisture tests to obtain semi-quantitative soil slurry saturation (S_f; defined here as the fraction of connected pore space filled by pig slurry), beneath three active storage ponds in southeastern Spain, developed on silty clay (pond 1), sandy loam (pond 2), and silt loam (pond 3). Twenty dipole–dipole ERT profiles were inverted in 2D using a smoothness-constrained (L2) inversion, and the resulting 2D models were stitched into 3D volumes for visualization and interpretation. Nine near-pond soil cores were analyzed to determine texture-specific porosity and to build calibration curves by incrementally wetting samples with pig slurry and normalizing resistivity to 25°C. In the modified Archie workflow, the cementation exponent (m) was selected per pond by minimizing cross-validated misfit within literature bounds, while the saturation exponent (n) and the reference resistivity at full saturation (ρ_o) were obtained from log–log regressions; pore-fluid resistivity (ρ_f) was measured on the pig slurry. Calibrated models indicate a textural control on infiltration: silty clay shows shallow influence with S_f declining below ~3 m; sandy loam exhibits deeper and laterally extensive percolation to ~4.5 m; silt loam is intermediate, maintaining elevated S_f to ~4–5 m. Across textures, resistivity increases sharply once S_f falls below the laboratory breakpoint thresholds $S_f \approx 0.37$, 0.48, and 0.28 for ponds 1–3, respectively (see Section 3.2), indicating a loss of continuous conductive pathways. These texture-specific thresholds were determined from laboratory resistivity–moisture curves as knee points marking the onset of an abrupt resistivity increase at low moisture and were converted from gravimetric moisture

Abbreviations: EC, electrical conductivity; ERT, electrical resistivity tomography; GMC, gravimetric moisture content; RMS, root mean square.

content to S_f using Equation (5). Because bulk resistivity depends on saturation and pore-fluid properties and m was fixed at its pond-level calibrated value, S_f maps are reported as semi-quantitative. The Archie-based approach offers a practical, non-invasive tool to locate likely leakage pathways and to prioritize targeted verification for risk management of slurry ponds.

Plain Language Summary

This study is focused on the detection of slurry infiltration and the prediction of soil water content in slurry storage ponds. An electrical resistivity tomography (ERT) method, which measures how the soil conducts electricity through it, was used to study three types of soil: silty clay, sandy clay, and clay. The objective was to calibrate the ERT data with laboratory tests to improve accuracy in measuring water content and detecting infiltration in slurry ponds. Field measurements in Murcia, Spain, showed that each soil type behaved differently. Silty clay limited infiltration to shallow layers, sandy clay allowed deeper infiltration, and clay retained water just below the pond with slow infiltration. The results demonstrate that ERT is a helpful tool for managing slurry storage, as it helps identify where infiltration occurs and how water content changes. This method provides valuable information for preventing soil and groundwater contamination in agricultural settings.

1 | INTRODUCTION

Intensive pig production has grown markedly over the past two decades to satisfy a steady rise in global pork consumption. The accompanying increase in slurry (a liquid mixture of feces, urine, and feed residues) poses a serious threat to soil and groundwater, especially in semi-arid regions where hydrological buffers are scarce (Ceretta et al., 2010; Maes et al., 2020). Field evidence from Brazil, Poland, and Russia shows that repeated land-spreading or accidental leakage of slurry enriches soils and shallow aquifers with nitrate, phosphate, copper, zinc, pathogens, and pharmaceutical residues, in some cases exceeding legal limits (da Rosa Couto et al., 2015; Mallmann et al., 2012; Marszałek et al., 2019; Otabbong et al., 2007). In southeastern Spain, where annual rainfall rarely exceeds 350 mm, unconfined aquifers commonly display nitrate (NO_3^-) concentrations above 50 mg L^{-1} after decades of slurry fertilization (Arbat et al., 2013; Díez et al., 2006; Margalef-Marti et al., 2021). Isotopic techniques have also been applied to trace specific sources of nitrate in groundwater, distinguishing pig slurry from other agricultural inputs (Margalef-Marti et al., 2021). The long-term use of pig slurry has been linked to increased soil salinity and electrical conductivity (EC) due to the accumulation of sodium and dissolved salts, particularly in Mediterranean soils (Díez et al., 2006).

Leakage through the bottoms of storage ponds is one of the least documented yet potentially most severe pathways for contaminants to enter the vadose zone. Pond floors are typically sealed with a compacted clay liner whose hydraulic performance declines as desiccation cracks and differential settlement develop, while thick crusts formed by evaporation may mask ongoing seepage. Once slurry escapes, its alkaline conditions (pH > 8), high ionic strength, and abundant ammonium accelerate carbonate dissolution, cation-exchange reactions, and redox shifts that weaken soil structure, increase salinization, and raise the risk of nitrous oxide emissions (Boitt et al., 2022; Jardé et al., 2007; Tóth et al., 2022). Moreover, the variability in slurry composition between farms and seasons, including fluctuations in pH, metal content, and antibiotic residues, can influence both environmental risk and the behavior of contaminants in subsurface transport. European legislation recognizes these hazards. The Nitrates Directive (91/676/EEC) and the Water Framework Directive (2000/60/EC) require Member States to implement measures that limit nutrient losses, while Royal Decrees 306/2020 and 47/2022 in Spain tighten the construction and monitoring standards for slurry ponds. This regulatory framework aligns with the 2030 Agenda for Sustainable Development, particularly Target 6.3 on improving water quality by reducing nutrient pollution (United Nations, 2015). Even so, operational, field-validated tools to verify pond-bottom integrity and depth of infiltration remain limited.

Electrical resistivity tomography (ERT) is well suited to this task. ERT injects low-frequency current through an electrode array and measures voltages to image bulk resistivity, governed mainly by moisture content, ion concentration, and porosity (Chambers et al., 2006; Kuras et al., 2016). The strong conductivity contrast between ion-rich slurry and the surrounding soil has been used to map seepage beneath lagoons (Martínez-Pagán et al., 2010) and tracking of seasonal changes in pond contents (Capa-Camacho et al., 2024). Advances in electrode design and data processing now enable high-resolution imaging, making ERT a valuable non-invasive tool for investigating infiltration dynamics and informing management. Inverted resistivity values alone do not directly yield soil slurry saturation (S_f) or gravimetric moisture content (GMC). Converting resistivity models into semi-quantitative S_f maps requires petrophysical calibration. Archie's law (Archie, 1942), relating resistivity, porosity, and soil slurry saturation, is widely applied, but surface conduction and variable pore geometry in clay-rich soils violate its original assumptions (Binley & Kemna, 2005; Merritt et al., 2016). Few studies have determined Archie parameters for Mediterranean slurry-affected soils, and, to our knowledge, none have explicitly coupled them with full three-dimensional ERT surveys of active storage ponds. In Mediterranean soils, slurry accumulation can alter pore structure and surface conduction, which affects ERT interpretation and calibration accuracy. In this study, a modified form of Archie's law with empirically derived parameters was applied to better represent conduction processes in slurry-affected clay-rich soils.

This study aims to (i) estimate soil slurry saturation (S_f) in the field from resistivity models calibrated against laboratory gravimetric moisture and (ii) assess potential slurry infiltration beneath storage ponds by integrating three-dimensional ERT with laboratory measurements of soil–slurry mixtures. Three ponds located on contrasting soil textures (silty clay, sandy loam, and silt loam) were surveyed, and the resulting resistivity models were correlated with laboratory-derived resistivity–moisture curves calibrated with modified Archie's law. This integrated approach offers a practical solution for monitoring slurry infiltration in semi-arid agricultural areas.

Core Ideas

- Electrical resistivity tomography (ERT) with lab data predicts soil water content and detects slurry infiltration in pig slurry ponds.
- The Archie model fits soil types: loamy clay (Pond 1), sandy clay (Pond 2), and clay (Pond 3).
- Detecting slurry infiltration helps prevent soil and groundwater contamination.
- Combines ERT and lab data, providing a tool for monitoring agricultural waste management.
- Explores soil effects on slurry infiltration, providing agricultural geophysics and moisture analysis.

2 | MATERIALS AND METHODS

2.1 | Study area

Fuente Álamo, in the Region of Murcia, Spain (Figure 1a,b), has a semi-arid Mediterranean climate. Temperatures typically vary between 15°C and 30°C, often exceeding 30°C during summer months. Annual rainfall ranges between ∼250 and 350 mm, concentrated in autumn and winter (García & Sarria, 2006; López Bermúdez et al., 2013). The municipality sits within the Betic Cordillera, an active orogen produced by the convergence of the African and Eurasian plates (Escosa et al., 2018). According to the 1:200,000 geological map of the Spanish Geological and Mining Institute (Instituto Geológico y Minero de España, IGME, 1993), bedrock comprises Mesozoic and Cenozoic (Paleogene–Neogene) limestones, dolomites, marls, and sandstones.

Soils are shallow, calcareous, and low in organic matter; according to the World Reference Base for Soil Resources (IUSS Working Group WRB, 2022), published by the Food and Agriculture Organization of the United Nations (FAO), they are predominantly Calcaric Regosols, consistent with regional descriptions. The investigation targeted three slurry ponds adjacent to pig farms near Fuente Álamo. Coordinates use ETRS89/UTM zone 30N, and pond characteristics are summarized in Table 1. Pond surfaces were classified by visual inspection as liquid or crusted; extensive crust formation in ponds 1 and 3 reflects strong evaporation and limited agitation (Figure 1c–e). Soil mapping was conducted using the regional 1:200,000 survey (IGME, 1993) and by hand auger sampling described in Section 2.2.

2.2 | Geophysical data collection

ERT is commonly used to image subsurface resistivity; the resulting contrasts can be related to variations in soil water content, contaminants, or subsurface features when interpreted with supporting information and calibration (Chambers et al., 2006; Helene et al., 2020; Holmes et al., 2022; Kuras et al., 2016; Reynolds, 1997). The electrical resistivity method involves injecting an electric current into the ground through a pair of current electrodes and measuring the resulting voltage difference between a pair of potential electrodes. Apparent resistivity is determined by combining this voltage difference, along with the known current, and a geometric factor (k), which is specific to the electrode configuration employed (Telford et al., 1990). The geometric factor

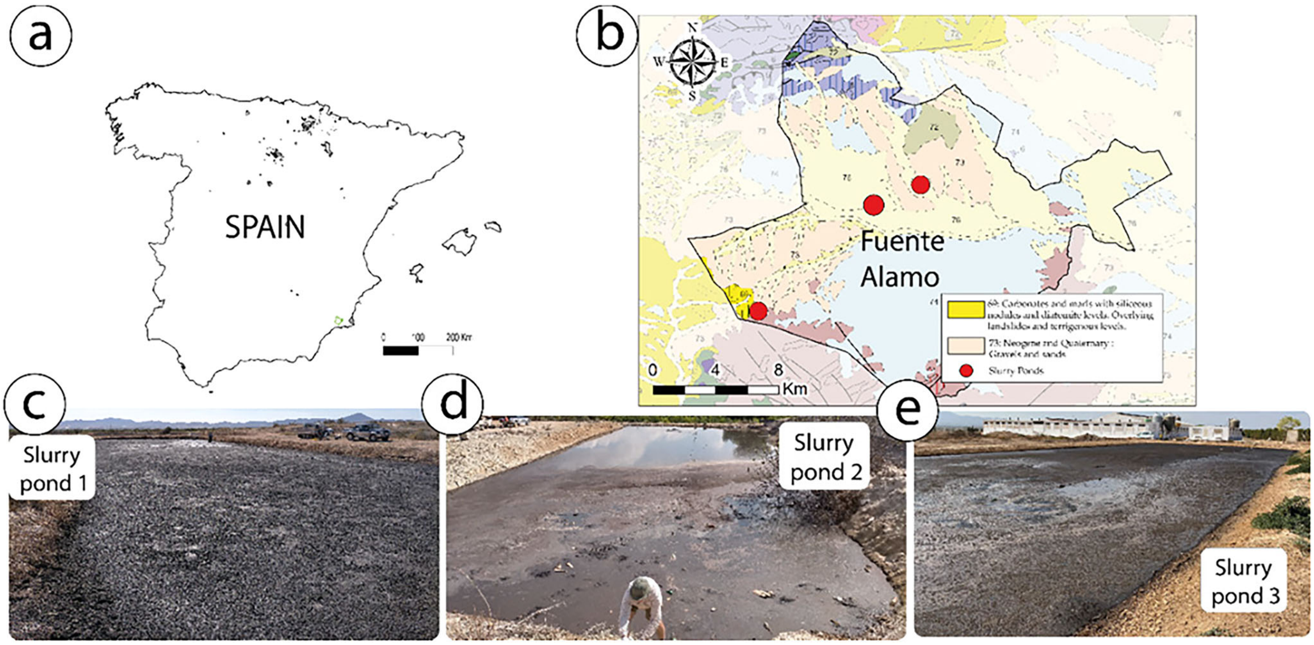

FIGURE 1 Study area showing (a) the location of Spain, (b) the locations of the three slurry ponds on the geological map of the Fuente Álamo municipality. Photographs show the condition of each pond at the time of measurement: (c) slurry pond 1, (d) slurry pond 2, and (e) slurry pond 3.

TABLE 1 Locations and physical characteristics of the pig slurry storage ponds.

Pond	UTM coordinates (ETRS89, Zone 30N)	Dimensions (m)	Slurry depth (m)[a]	Surface condition
1	658,150 m E, 4,180,050 m N	17 × 54	0.75	Crusted
2	649,845 m E, 4,171,830 m N	15 × 52	1.00	Mixed (liquid east; crusted west)
3	656,350 m E, 4,178,650 m N	14 × 42	0.50	Crusted

Note: The wet length of the pole was measured at each point and then averaged.

[a]Depths were estimated in situ using a wooden pole inserted at five locations (center and near each corner).

accounts for the spatial arrangement of the electrodes in field applications and converts the measured resistance to apparent resistivity.

The subsurface resistivity distribution is evaluated by using forward modeling and inversion techniques. These computational procedures iteratively adjust a resistivity model until the calculated responses match the measured data to a predefined misfit target based on the data-error model (Binley & Kemna, 2005; Loke & Barker, 1996; Tso et al., 2017). Figure 2 summarizes the workflow from acquisition to calibration. Field measurements inside and outside the ponds were inverted in 2D (profile-by-profile) using a smoothness-constrained (L2) inversion to obtain resistivity models. The resulting 2D inverted sections were then stitched into a 3D volume for visualization and interpretation. Soil samples collected near the ponds were analyzed in the laboratory to determine physical properties and to calibrate modified Archie's law. The calibrated relationship was applied to inverted resistivity models to estimate soil slurry saturation (S_f).

2.3 | Electrical resistivity measurements

In September 2021, ERT surveys were conducted at three slurry ponds using a dipole–dipole configuration. Injected currents ranged from 50 to 200 mA and average contact resistance was <1 kOhm. The setup was deployed both inside and outside each pond to compare the electrical resistivity of the slurry with the surrounding soil and to identify potential infiltration pathways. Internal (floating) lines used AGI passive graphite electrode cables (marine-grade, waterproof multiconductor with embedded graphite sockets), held at the slurry surface using polyethylene floats and plastic clamps. External (land) lines used AGI Active Electrode Cables installed directly in the ground. Both internal and external lines had 28 electrodes at 2 m spacing, yielding 54 m-long survey lines. Profiles were aligned along the longitudinal axis of each pond to allow coherent data integration for 3D modeling. Their layout was adapted to the geometry of each pond to ensure full spatial coverage. In total, slurry pond 1 included seven pro-

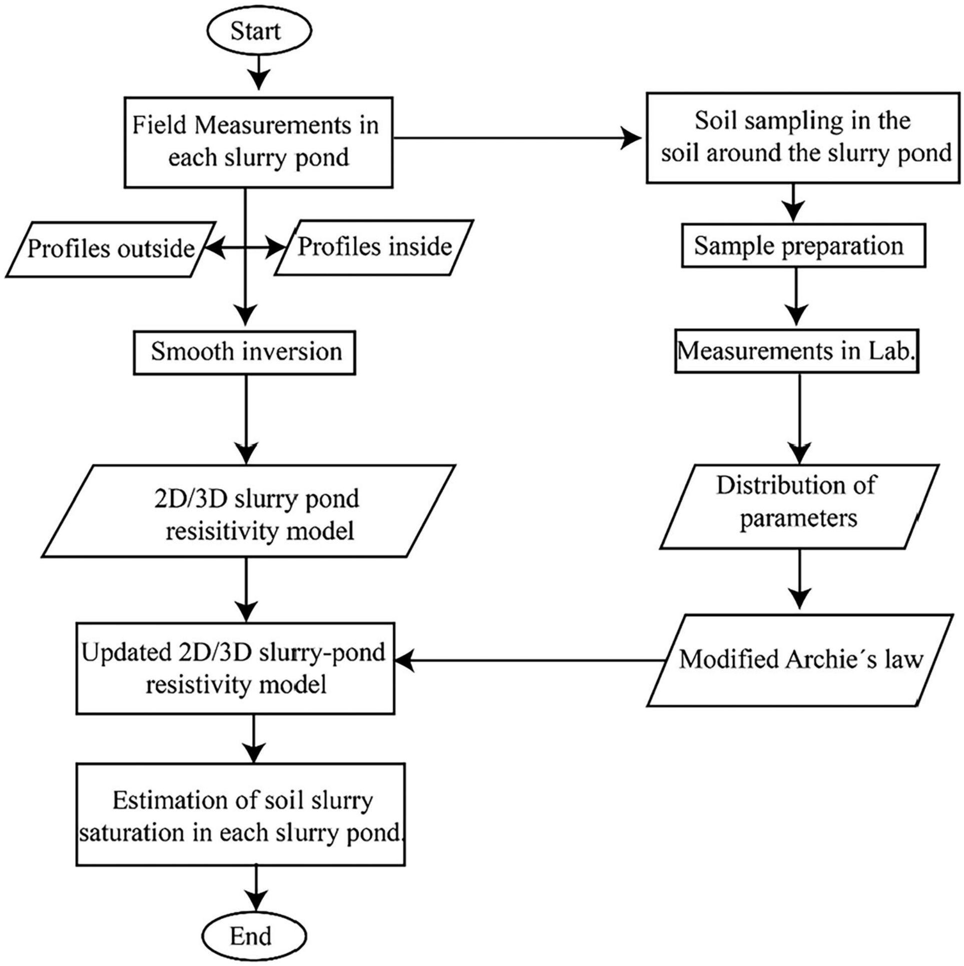

FIGURE 2 Workflow from field electrical resistivity tomography (ERT) acquisition to calibration of modified Archie's law for estimating soil slurry saturation (S_f).

files (four external, three internal), pond 2 had six (three of each type), and pond 3 also included seven profiles.

The dipole–dipole array was chosen for its high lateral resolution, suitable for detecting lateral conductivity variations; vertical sensitivity is lower than for Wenner or Schlumberger arrays, which can blur sharp boundaries (Corwin & Lesch, 2013; Dahlin & Zhou, 2004). Measurements were collected with an AGI SuperSting R8 and processed in EarthImager v2.8.0. The workflow included outlier removal for measurements with contact resistance ≥5000 ohms and visual inspection of noisy data, defined below. Individual 2D inversions were performed for each of the 20 profiles and were inverted in 2D (profile-by-profile) and then stitched into 3D volumes for visualization and interpretation. An L2 smoothness-constrained inversion was applied with the following settings: up to eight iterations, a target root mean square (RMS) misfit ≤10%, and an error reduction threshold of 5%. Both the smoothness and damping factors were set to 10, and the noise level was set to 3%. Although less precise at delineating sharp boundaries, the smooth inversion approach performs better in conductive and noisy environments such as slurry ponds (Binley & Kemna, 2005). The initial model was based on the average apparent resistivity, constrained between 1 and 100,000 Ω.m. The inversion routine employed up to six conjugate gradient iterations per step, a resolution factor of 0.2, and a horizontal-to-vertical roughness ratio of 0.5 to regulate model regularization. RMS error values for the 20 profiles ranged from 4.6% to 9.8%, with an average of 6.2%. Final 2D resistivity models and soil slurry saturation (S_f) maps were generated using Surfer v.25.4.320 to visualize lateral and vertical distributions.

2.4 | Development of laboratory-based petrophysical relationships

Nine soil cores (n = 3 per pond) were collected adjacent to each pond perimeter at 0–20 cm below ground surface using a 5-cm-diameter hand auger. The surface was cleared prior to augering and intact cores were carefully extracted

TABLE 2 Sample-level porosity, dry bulk density, and pond-level Archie calibration parameters.

Pond	Samples	Porosity (%)	Bulk density gcm^{-3}	m (-)	N (-)	ρ_o (Ohm.m)	ρ_f (Ohm.m)	F (-)
Pond 1 (silty clay)	1	52	1.16	2.10	2.10	1.85	0.38	4.87
	2	54	1.2					
	3	56	1.24					
Pond 2 (sandy loam)	4	46	1.26	2.20	2.50	3.25	0.44	7.38
	5	47	1.3					
	6	48	1.34					
Pond 3 (silt loam)	7	54	1.16	1.50	2.10	1.42	0.54	2.64
	8	56	1.2					
	9	58	1.24					

Note: Porosity and bulk density are reported per sample; pond-level Archie parameters are listed once per pond. ρ_f (slurry) measured at 25°C. ρ_0 from the log–log intercept. Porosity computed with particle density $\rho_p = 2.65$ g cm^{-3}. m constrained to the literature-reported range 1–3 and selected per pond by misfit minimization (see Section 2.4); n is from the slope of the log–log regression log $(\rho_r/\rho_o) = -n$ log(s_f) (see Section 2.5). Unless stated otherwise, values are pond-level estimates.

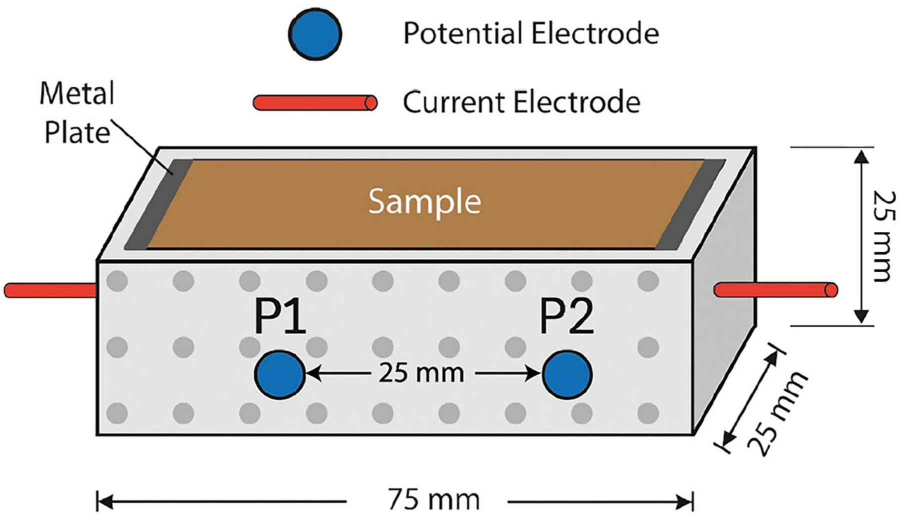

FIGURE 3 Schematic representation of the coffin used for laboratory resistivity measurements.

to minimize compaction; samples were immediately sealed to preserve in situ moisture and structural integrity. Porosity and dry bulk density are reported per sample and as mean ± standard deviation per pond (Table 2). Archie parameters were calibrated at the pond level: m was constrained to the literature-reported range 1–3 (Glover, 2016; Kazemzadeh et al., 2007) and selected per pond as the value minimizing cross-validated misfit of the laboratory resistivity-S_f pairs, n was obtained from a log–log regression using all laboratory points for that pond; ρ_o was estimated from the intercept of the log–log regression (Equation 7).

Pore-fluid resistivity ρ_f was measured on pig slurry at 25°C. For laboratory resistivity measurements, samples were transferred into custom plastic holders ("coffins") measuring 25 × 25 × 75 mm (Figure 3). Because the 5-cm-diameter core exceeded the cell cross-section (25 × 25 mm), air-dry soil was gently disaggregated and repacked into the 25 × 25 × 75 mm cell to match the field bulk density (ρ_{bfield}). A target mass was used (mt = ρ_{bfield}, × V_{cell}), hand-tapping only (no mechanical compaction), and the packed density was verified within ± 5% of ρ_{bfield}; out-of-tolerance specimens were re-prepared. Initial GMC and bulk density were determined on separate sacrificial aliquots using standard oven-drying and volumetric methods.

Each coffin included two current electrodes (one at each end) and two centrally placed potential electrodes spaced 25 mm apart. Pig slurry was added incrementally to simulate progressive saturation, and each stage was designed to reflect realistic infiltration scenarios occurring beneath storage ponds. After each addition, samples equilibrated for 24 h under controlled temperature and humidity conditions, which were monitored and later used to correct resistivity readings.

Apparent resistivity was plotted against GMC to develop empirical calibration curves for each sample. These curves supported the parameterization of modified Archie's law and the semi-quantitative interpretation of field ERT sections in terms of soil slurry saturation (S_f), assuming a representative bulk density for each pond area. Soil texture was classified using a laser diffraction analyzer (Mastersizer 2000LF) according to the FAO-ISRIC system (Baxter, 2007). Soil groups were categorized as silty clay (pond 1), sandy loam (pond 2), and silt loam (pond 3), consistent with FAO classifications (FAO, 2006).

Measurements were performed using a SYSCAL R1 Plus resistivimeter (IRIS Instruments) with a standard four-electrode configuration. The fixed geometry of the setup ensured reliable, repeatable measurements and minimized the influence of local heterogeneities (Kazemzadeh et al., 2007). Since temperature significantly affects resistivity, ambient temperatures (21°C–26°C) were recorded and used to apply corrections using the equation from Hayley et al. (2010).

$$\rho T = \rho_{\text{measured}} \; [1 + 0.02\,(T - 25)] \tag{1}$$

where ρT is the temperature-corrected resistivity (Ohm.m), ρ_{measured} is the raw resistivity reading from the instrument, and T is the temperature (°C). The correction was normalized to 25°C. This approach enabled the construction of soil-specific resistivity, GMC calibration curves, which were later used for qualitative interpretation of field resistivity profiles.

The physicochemical analysis of soil EC was carried out on air-dried soil samples, previously sieved to <2 mm. Soil EC was measured in a 1:5 (w/v) soil:deionized water suspension using selective electrodes (Andrades, 1996). Measurements were performed with a portable multiparameter meter (HANNA Instruments HI 9025) on homogenized suspensions, and EC values were recorded once the reading stabilized. All measurements were standardized to 25°C.

2.5 | Calibration of ERT models

A modified form of Archie's law, originally developed for clean sandstones (Archie, 1942), was used in this study to relate bulk resistivity to soil slurry saturation (S_f). The calibration was empirically adjusted for each soil texture to partially capture effects of pore connectivity and surface conduction typical of clay-rich or slurry-affected soils. This calibration enables semi-quantitative mapping of relative variations in soil slurry saturation (S_f) within each pond, with qualitative inter-pond comparisons referenced to the texture-specific laboratory thresholds. Here S_f denotes the fraction of connected pore space filled by pig slurry (pore fluid) estimated from bulk resistivity; the pore-fluid resistivity, ρ_f corresponds to the slurry measured at 25°C. The symbol S_f is used in place of the conventional water-specific S_w.

The modified form of Archie's law applied here is:

$$\rho_r = a\,\rho_f \times \phi^{-m} \times S_f^{-n} \tag{2}$$

here, a is the Archie tortuosity factor. In this study, a was fixed to 1 (Reynolds, 1997), and its effect is treated as part of the pond-specific calibration (ρ_o and F) obtained from the laboratory regressions.

Note that ρ_r is the bulk resistivity of the soil sample (Ohm.m), ρ_f is the pore-fluid resistivity of the pore fluid, ϕ is the soil porosity, m is the cementation exponent, S_f is the soil slurry saturation, and n is the saturation exponent. The fluid resistivity ρ_f was measured in the laboratory using a conductivity probe at 25°C. The porosity ϕ was calculated from the dry bulk density ρ_b and particle density ρ_p using the equation:

$$\phi = 1 - \frac{\rho_b}{\rho_p} \tag{3}$$

Field bulk density was determined gravimetrically from oven-dry mass and core volume. Particle density was not measured directly; the standard mineral-soil value (ρ_p = 2.65 g cm^{-3}) was used to compute porosity. Sample preparation and packing to match field bulk density (±5%) are described in Section 2.4.

The GMC at each wetting step was calculated as follows:

$$\text{GMC} = \frac{m_w - m_d}{m_d} \tag{4}$$

GMC is defined as a gravimetric mass ratio (g g^{-1}). When expressed as a percentage, GMC (%) = 100 × GMC. Where m_w is the wet mass of the soil, and m_d is the dry mass. This method aligns with ISO 11,465 and FAO moisture determination protocols, offering higher standardization (Margesin & Schinner, 2005).

The soil slurry saturation S_f was then derived as follows:

$$S_f = \frac{\text{GMC} \times \rho_b}{\phi} \tag{5}$$

where ρ_b is the dry bulk density of the soil (g cm^{-3}).

Cementation exponent (m): Consistent with Section 2.4, m was estimated from the calibration data but constrained to 1–3 based on published bounds (Glover, 2016; Kazemzadeh et al., 2007).

To determine the saturation exponent n and the reference resistivity at full saturation (ρ_o), a logarithmic transformation of the relationship between bulk resistivity and soil slurry saturation was applied:

$$\rho_r = \rho_o \times S_f^{-n} \tag{6}$$

Taking logarithms on both sides yields a linear equation:

$$\log\left(\rho_r\right) = -n\log(S_f) + \log(\rho_o) \quad (7)$$

Equation (7) is fitted by linear regression over all laboratory points; n is the slope and ρ_0 the intercept. From Equation (7), n is obtained from the negative slope of the best-fit line and $\log \rho_o$ from the intercept, using ordinary least-squares regression over all laboratory (S_f, ρ_r) pairs for each pond (25˚C). ρ_o is then obtained by back-transformation. The resulting n and ρ_o were used to interpret the ERT field models.

The formation factor was computed as follows:

$$F = \rho_o/\rho_f \quad (8)$$

which relates the fully saturated bulk resistivity to the pore-fluid resistivity.

Modified Archie models have been proposed to integrate surface conduction and pore connectivity effects, particularly in slurry-affected clays (Choo et al., 2022; Hashemi et al., 2021). In clay-rich or saline soils, deviations from Archie's assumptions may occur due to surface conduction and pore geometry complexity. Therefore, interpretations were limited to relative rather than absolute saturation values (Binley & Kemna, 2005; Merritt et al., 2016).

2.6 | Transformation of field inversions to S_f maps

Inverted resistivity grids (ρ_r, Ohm.m) exported from EarthImager v2.8.0 (2D inversions) were corrected to 25˚C using the same temperature-correction scheme applied in the laboratory calibrations. Each cell was then calibrated with the pond-specific Archie parameters (Table 2). Soil slurry saturation (S_f) was computed for every cell by rearranging the modified Archie's law:

$$S_f = \left[\left(a \times \rho_f \times \phi^{-m}\right)/\ \rho_r\right)\right]^{\frac{1}{n}} \quad (9)$$

where ρ_r is the inverted bulk resistivity at 25˚C (Ohm.m), ρ_f is the pore-fluid resistivity at 25˚C (Ohm.m), ϕ is porosity, m is the cementation exponent, and n is the saturation exponent. Laboratory-derived, pond-level values were used for ρ_f, ϕ, m, and n. All cells fell within the laboratory calibration range; resulting S_f values were ≤0.98, so no clipping above unity was required. Maps were generated and post-processed in Surfer (Golden Software).

Operational saturation thresholds (S_f) were defined from the laboratory ρ–GMC datasets as the breakpoint between two regimes: (i) a connected high-moisture regime in which electrolytic conduction dominates and resistivity varies smoothly with moisture, and (ii) a low-moisture regime in which pore-fluid connectivity progressively decreases and resistivity increases sharply. The breakpoint was estimated on the measured datasets by fitting a two-segment model in log-log space and selecting the breakpoint that minimized the total residual sum of squares. The corresponding GMC value was then converted to S_f using Equation (5) with pond-specific ρ_b and ϕ.

3 | RESULTS AND DISCUSSION

3.1 | Electrical resistivity measurements in the field

The set of unadjusted stitched 3D volumes derived from 2D ERT inversions showed broader and deeper low-resistivity zones where perched liquid is inferred. Specifically, pond 2 exhibited the widest and deepest conductive body, pond 1 (silty clay) showed shallow conductivity that faded below ∼3 m, and pond 3 (silt loam) was intermediate with patchy conductors at ∼3–5 m. These unadjusted resistivity contrasts primarily reflect pore-fluid conductivity and saturation, rather than clay content alone. These results correspond to unadjusted inversions of the dipole-dipole ERT profiles and therefore do not yet incorporate laboratory calibration or Archie's law parameters; the temperature-normalized resistivity sections and the derived semi-quantitative S_f maps obtained from the laboratory calibration are presented in Section 3.2.

The resistivity models for all three ponds revealed two principal zones (Figure 4): a low-resistivity zone, 0.1–13 Ω.m (blue–green), interpreted as the slurry body and saturated shallow soils within the pond footprint; and a high-resistivity zone, >18 Ω.m (red), corresponding to pond walls and surrounding drier soils. Field observations recorded free-standing (uncrusted) liquid versus crusted surfaces within the ponds and noted dry, elevated berms with sparse vegetation at the margins. Free-standing liquid areas at the pond surface corresponded to ∼0.1–3 Ω.m, crusted/semi-dried slurry to ∼4–11 Ω.m, and dry berms/surrounding soils to >18 Ω.m. For example, slurry zones with a free-standing (uncrusted) liquid surface showed ∼0.1–3 Ω.m, whereas crusted or semi-dried zones showed ∼4–11 Ω.m. This variation aligns with the stratification observed in ponds 1 and 3, which had partially crusted surfaces, as well as with reports by Capa-Camacho et al. (2024), who documented similar variability in slurry resistivity based on fluid consistency. The higher resistivity zones near the edges of each model are interpreted as drier, unsaturated soils or compacted berms forming the pond boundaries. These zones corresponded to visual inspections of elevated, dry edges and vegetation presence.

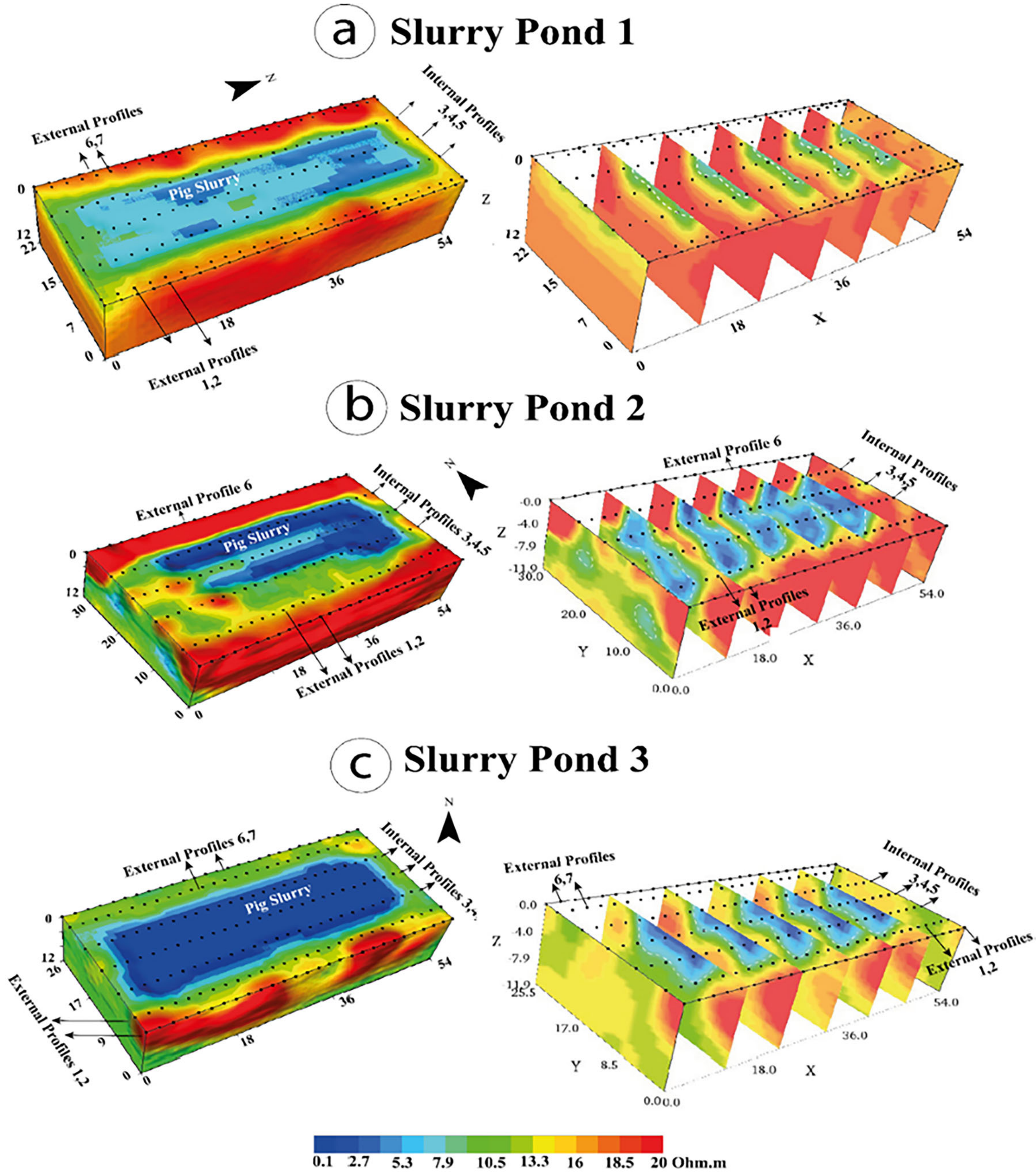

FIGURE 4 Composite 3D visualization of stitched 2D electrical resistivity tomography (ERT) inversions for the three slurry ponds: (a) pond 1, (b) pond 2, and (c) pond 3.

Although the resistivity of unconsolidated soils is heavily influenced by the type and saturation of pore fluids, in this context, both reduced saturation and slurry infiltration appear to control lateral contrasts. These inversion results showed consistent patterns. For the 2D inversions, RMS errors ranged from 4.6% to 9.8% (mean 6.2%), supporting their use for preliminary interpretation. Data were inverted in 2D (profile-by-profile) in EarthImager v2.8.0 with an L2-norm (least-squares) smoothness constraint.

Slurry depth was previously estimated using a wooden pole inserted manually at five points per pond (Section 2.1). While these in situ depth measurements serve as reference values (0.5–1.0 m), the resistivity models display apparent non-uniform depth patterns. These undulations likely reflect infiltration pathways, variations in slurry density, or bottom compaction and inversion smoothing, and array geometry may also contribute to apparent undulation, rather than an accurate geometric representation of the pond bottom. RMS misfits for the 2D inversions were 4.6%–9.8% (mean 6.2%); inversions used an L2 smoothness constraint (see Section 2.3). Calibrated models in Section 3.2 further examine depth-dependent saturation (S_f).

3.2 | Laboratory measurements and model calibration results

Laboratory measurements suggest that pig slurry consistently exhibited lower electrical resistivity than soil samples, with values ranging from 0.38 to 0.55 Ω.m at 25˚C. These results are consistent with those reported by Bonmatí et al. (2003) and reflect the highest water content (93%–98%) and ionic strength of pig slurry. In contrast, unsaturated laboratory soils displayed significantly higher resistivity (>13 Ω.m), with soil EC (1:5 soil:water extract) values of 0.34–1.32 mS cm^{-1} and pH 8.02–8.32, consistent with lower saturation and solute concentrations. Bulk electrical resistivity in soil reflects both pore connectivity (related to texture and structure) and pore-fluid conductivity. In general, the decrease in resistivity with increasing moisture is more pronounced when pore fluid has higher ionic strength; in these experiments, the conductive slurry presents this behavior at higher GMC. Based on particle-size distributions, the soil of slurry pond 1 (15% sand, 40% silt, 45% clay) is classified as silty clay; pond 2 (51% sand, 45% silt, 4% clay) as sandy loam; and pond 3 (34% sand, 52% silt, 14% clay) as silt loam. These textures match those reported in other Mediterranean pig-farming regions, where calcareous soils exhibit variable responses to salinity and slurry infiltration (Bernal, Roig, Lax, et al., 1992).

Initial laboratory resistivity values reflected these textures: the coarser sandy soil (pond 2) had the highest resistivity (68.6 Ω.m at 10% GMC), while the clay-rich soil (pond 1) and the silt-rich soil (pond 3) showed lower initial values (53.9 Ω.m at 7% GMC and 55.1 Ω.m at 6% GMC, respectively). These trends reflect the combined electrolytic and surface-conduction pathways, the latter being especially relevant in finer-textured soils, under partial saturation or variable electrolyte concentration (Datsios et al., 2017; Merritt et al., 2016). Clay-rich soils support surface conduction due to their high cation exchange capacity, and silt-rich soils retain more water and exhibit higher pore tortuosity; both mechanisms result in lower resistivity even under moderately dry conditions (Horváth et al., 2021; Revil et al., 1998). As described in Section 2.4, pond-specific slurry and laboratory measurements were used to derive the petrophysical calibration parameters. These experiments yielded soil-specific Archie calibration parameters. Laboratory resistivity was plotted against GMC, producing non-linear calibration curves consistent with a power-law relationship. Although originally formulated for clean, brine-saturated sandstones (Archie, 1942), the modified Archie's law provided good empirical fits in this context (R^2 = 0.71–0.83 across ponds).

Figure 5 shows laboratory-calibrated regression curves obtained using modified Archie's law, fitted separately for each soil. The calibration links laboratory electrical resistivity to GMC using parameters derived from empirical measurements, including porosity, bulk density, and pore-fluid conductivity. Each curve represents the best-fit relationship between laboratory resistivity values and GMC for soils from ponds 1 (silty clay), 2 (sandy loam), and 3 (silt loam). The equations displayed summarize these texture-specific regressions. To estimate the initial petrophysical parameters, soil samples were analyzed before slurry addition to characterize electrical baseline and physical properties. Porosity (ϕ) was calculated from the bulk density of air-dried samples, assuming a standard particle density of 2.65 g cm^{-3}. Overall, silty clay and silt loam were slightly more porous than sandy loam (Table 2).

The formation factor (F; Equation 8) was highest in pond 2, intermediate in pond 1, and lowest in pond 3 (Table 2). This ordering follows from Equation (8): pond 2 combines a higher ρ_o with a moderate ρ_f; pond 1 an intermediate ρ_0 with a low ρ_f, and pond 3 the lowest ρ_o with the highest ρ_f (Table 2). In finer-textured soils (silty clay, silt loam), surface-conduction effects depress ρ_0 at saturation, lowering F even when tortuosity increases (Alam et al., 2010). The saturation exponent (n) was obtained as described in Section 2.5, whereas the cementation exponent (m) was constrained and selected per pond as in Section 2.4. The resulting ranges m = 1.50–2.20; n = 2.10–2.50 are typical of soils containing fines and moderate compaction (Binley & Kemna, 2005; Du et al., 2021; Revil et al., 1998; Tiab & Donaldson, 2003). This is consistent with the porosity ordering (pond 2< pond 1 $\lesssim$ pond 3) and the resulting F sequence (pond 3 < pond 1 < pond 2). These results show two key points: first, that Archie-type models can be adapted to slurry-impacted soils when parameters are empirically constrained by texture; and second, that although Archie's original assumptions are typically better satisfied in coarser, low-clay materials, the empirical power-law fit used here performs best for ponds 1 and 3 (R^2 = 0.83 and 0.79) and more weakly for pond 2 (R^2 = 0.71), with larger residuals at low GMC (≈15%–20%). Therefore, Archie-derived saturation estimates are treated as semi-quantitative, particularly in the low-moisture regime. Thus, texture not only governs the depth and geometry of infiltration but also controls the reliability of Archie-derived saturation estimates.

Figure 5a–c show that residuals increase, and the modified Archie fit deteriorates at very low moisture (∼15%–20% GMC), consistent with loss of hydraulic connectivity and a proportionally greater role of surface conduction under partial saturation (Abu-Hassanein et al., 1996). Additional experimental factors (packing-induced voids at the electrode–soil interface and local salt redistribution/precipitation) may also affect low-moisture readings (Bernal, Roig, Madrid, et al., 1992; de Cássia Goulart Ferreira et al., 2021). This deterioration is consistent with the well-documented non-universality of Archie's law (Glover, 2016), where formation factors and exponents vary with pore geometry and clay-related surface conduction. At higher moisture (higher GMC/higher S_f), electrolytic conduction is expected to dominate, and the mod-

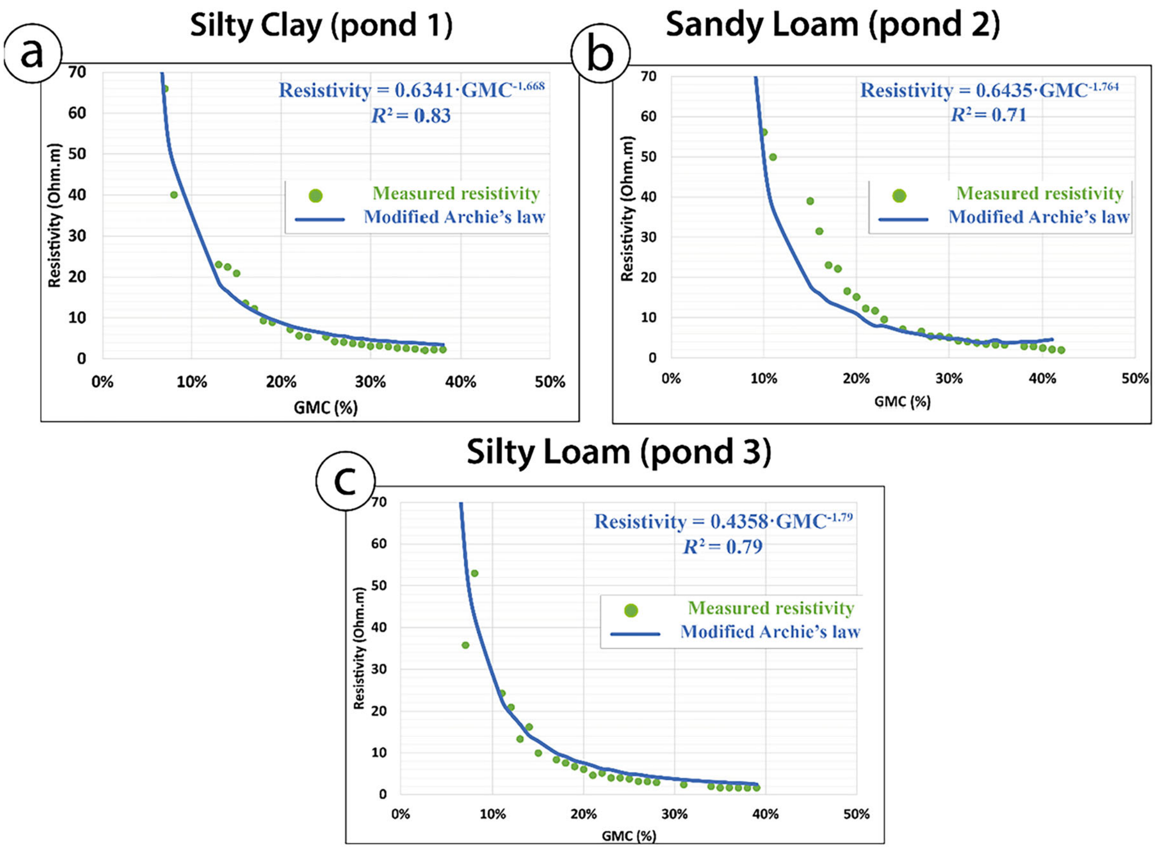

FIGURE 5 Laboratory calibration curves relating electrical resistivity to gravimetric moisture content (GMC) for soils from ponds 1–3 (a–c). Green points are laboratory measurements during progressive wetting with incremental additions of pig slurry; blue lines are regressions fitted to modified Archie's law.

ified Archie regressions show their best overall performance (R^2 = 0.71–0.83). Across textures, the resistivity–moisture relation is inverse and non-linear, but the fitted responses differ among soils. Based on Figure 5, silty clay (pond 1) shows the least steep power-law exponent (≈ −1.67), whereas sandy loam (pond 2) and silt loam (pond 3) show steeper and similar exponents (≈ −1.76 to −1.79). Although the exponents for ponds 2 and 3 are similar, the governing mechanisms may differ: sandy loam tends to decline more sharply with increasing GMC due to faster connectivity gains, whereas in silty clay, surface conduction likely lowers resistivity even at moderate moisture, making the overall response appear closer to that of coarser material. Silt loam (pond 3) shows comparatively lower resistivity across much of the GMC range and the steepest fitted exponent (Figure 5), indicating high electrical sensitivity to wetting in the laboratory. This laboratory sensitivity does not directly imply greater field infiltration; in the field, pond 3 shows an intermediate depth/continuity of elevation S_f relative to ponds 1 and 2, which is primarily controlled by hydraulic properties, pond recharge conditions, and heterogeneity. Accordingly, resistivity is expected to decrease with increasing moisture (higher GMC/higher S_f), but should not be interpreted as a direct indicator of slurry concentration; instead, it reflects the combined effects of soil structure, texture, and pore-fluid conductivity. Liu et al. (2008) similarly cautioned that electrical resistivity in agricultural soils is controlled by both water content and solute concentration, noting that changes in pore-fluid conductivity can mimic moisture effects. Taken together, these observations suggest that Archie-type models are suitable for semi-quantitative estimates at high GMC/S_f, with caution warranted under partial saturation, particularly in fine-textured soils.

For each soil type, three replicate samples were analyzed; variability was low (coefficient of variation <10%) for porosity ϕ and dry bulk density, and pond-level parameters *(F, n,* and ρ_o) showed narrow dispersion and good fits (Figure 5; Table 2). Operationally, two regimes are distinguished for applying the calibration: (i) a high-moisture domain (higher GMC/higher S_f), in which quantitative estimates are warranted (R^2 = 0.71–0.83), and (ii) a low-GMC domain (≈ 15%–20% GMC; pond-dependent), in which results should be treated qualitatively as an early-warning indicator of reduced pore-fluid connectivity in the laboratory calibration. Consistent with this two-regime behavior, the laboratory datasets show knee points at low GMC. The knee points occur at approximately GMC ≈ 0.17 (pond 1), 0.18 (pond 2), and 0.13 (pond 3). Using Equation (5) with pond-specific ρ_b and ϕ (Table 2), these correspond to $S_f \approx 0.37$, 0.48, and 0.28, respectively (threshold definition in Section 2.6). This two-regime interpretation aligns with agrogeophysical studies: Kelly et al. (2011) used 2D ERT to optimize soil moisture sensor placement for irrigation scheduling, while Araya Vargas et al. (2020) found that resistivity monitoring effectively detects infiltration heterogeneity and deep percolation in vineyards. Innocenti et al. (2024) showed that time-lapse ERT non-invasively tracks irrigation water flow and identifies preferential pathways. Combined with in situ moisture monitoring, these regimes can inform reapplication timing and irrigation management. The Archie parameters reported here are empirically constrained for three soil textures from a single semi-arid Mediterranean setting (SE Spain). Because Mediterranean slurry-affected soils span wider textural/mineralogical ranges and slurry chemistry can vary seasonally, these parameter ranges (m, n, ρ_o, and F) should not be assumed transferable without local calibration.

3.3 | Soil slurry saturation from pig slurry infiltration

The apparent reduction of near-surface contrast after conversion reflects the non-linear remapping from ρ to S_f (Equation 9); no additional spatial smoothing was applied beyond inversion regularization. Figures 6–8 show unadjusted field inverted resistivity (left) and temperature-normalized (adjusted) resistivity at 25°C (right) for ponds 1–3. These adjusted sections improve interpretability; the S_f estimates are obtained by applying the laboratory calibration (Equations 2, 6–7, and 9) and are summarized in Figure 9. The calibration emphasizes saturation-related trends; the reduced near-surface contrast is a remapping effect and should not be interpreted as noise removal.

The calibrated profiles reveal more vertically continuous structures, consistent with downward migration of pig slurry; however, regularization may also enhance apparent continuity, so these features are interpreted cautiously. In pond 1 (silty clay), shallow low resistivity maps to elevated S_f that attenuates by ∼3.0 m. In pond 2 (sandy loam), adjusted resistivity and derived S_f show lateral spreading along the pond base and persistence to ∼4.5 m. In pond 3 (silt loam), elevated S_f accumulates at ∼1.7–4.5 m and becomes more discontinuous below, indicating an intermediate field infiltration response (depth/continuity) relative to ponds 1 and 2.

From these resistivity models, soil slurry saturation S_f was estimated using the modified Archie relation (Equation 2) with texture-specific parameters and pond-level constants (Equation 9). Figure 9 presents modeled S_f at five depth intervals. The highest values (70%–90%) occur at 0.5 m within pond footprints. At 1.7 m, S_f remains elevated beneath the ponds (notably ponds 1 and 3, ∼50%–70%). Peripheral areas show low S_f (10%–30%), consistent with background moisture. At greater depths (3.0–6.3 m), S_f declines overall, with persistence in pond 2 to ∼4.5 m and in pond 3 to ∼4–5 m, while pond 1 falls below ∼3 m. This stratified pattern suggests infiltration fronts modulated by texture, porosity, and retention capacity. These estimates assume stable pore-fluid resistivity ρ_f and are most reliable in the high-GMC/high-S_f regime; they are semi-quantitative.

In Pond 2 (sandy loam), near-surface resistivity is low across most of the section (∼0.1–3 Ω.m) and remains relatively low at 1.7–3.0 m, with lateral spreading along the pond base; higher-resistivity frames mark berms and drier margins. At 4.5–6.3 m, resistivity increases toward background. The corresponding S_f (Figure 9) indicates high saturation at 0.5–1.7 m and a gradual decline with depth, consistent with mixed vertical and lateral infiltration in coarser soils (Schwartz et al., 2008).

Differences among ponds are consistent with their distinct soil textures. In pond 1 (silty clay), high saturation is confined to the upper layers and decreases by ∼3.0 m, indicating limited vertical continuity in the finer matrix. In pond 2 (sandy loam), elevated saturation persists deeper and spreads laterally along the pond base, persisting to ∼4.5 m consistent with more efficient vertical and lateral infiltration in coarser material. In pond 3 (silt loam), the response is intermediate: saturation is elevated at ∼1.7 m, becomes more variable around 3.0 m, and approaches background by ∼6.3 m. These semi-quantitative S_f estimates are consistent with the laboratory-derived operational thresholds (Section 3.2). For example, in pond 2 (sandy loam), S_f remains above the 48% threshold down to ∼4.5 m, whereas in pond 1 (silty clay), it falls below the 37% threshold by ∼3 m, indicating limited vertical continuity.

Field application of the modified Archie approach assumes relatively stable pore-fluid conductivity and uniform petrophysical parameters; therefore the S_f maps are semi-quantitative and most reliable in the high-moisture regime (see Section 2.5). Consequently, the saturation maps are semi-quantitative: bulk resistivity responds to both moisture and ionic strength, and surface-conduction effects in fine-textured soils can mimic high water content during drying–rewetting cycles (Oh et al., 2014). Additional factors (solute accumulation, conductivity heterogeneity, capillarity) also influence the patterns. Despite these limitations, the agreement between modeled saturation profiles and expected hydraulic behavior across textures supports the practical value of the calibration. Inference of slurry-affected zones should be confirmed where possible with chemical data, but ERT combined with texture-specific, modified-Archie calibration remains a useful tool for mapping subsurface saturation in pond operations; recent extensions of Archie-type models further reinforce its semi-quantitative utility (Fu et al., 2021).

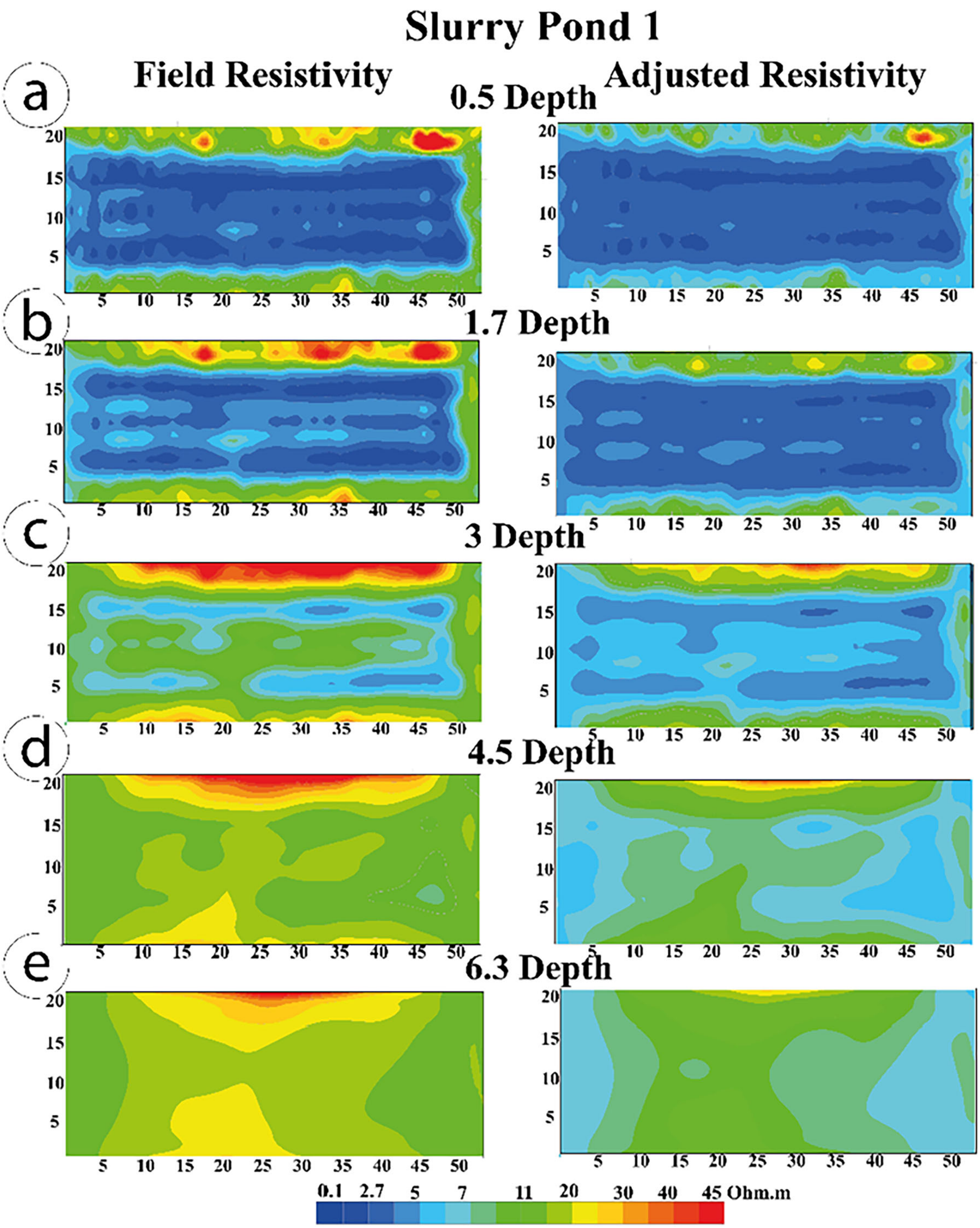

FIGURE 6 Horizontal slices for Pond 1: (left) unadjusted inverted resistivity; (right) Archie-calibrated resistivity sections. Depths: (a) 0.5 m, (b) 1.7 m, (c) 3.0 m, (d) 4.5 m, (e) 6.3 m.

The plan-view S_f slices (Figure 9) indicate that infiltration depth and geometry follow a first-order control by subsoil texture. Beneath pond 1 (silty clay), saturation declines rapidly below ∼3 m, indicating limited vertical continuity and confinement of elevated saturation to shallow layers. By contrast, pond 2 (sandy loam) retains elevated saturation to ∼4.5 m and shows broader lateral spreading along the pond base, consistent with more efficient vertical and lateral infiltration in coarser material. Pond 3 (silt loam) shows an intermediate response: high saturation persists to ∼4–5 m and then breaks into discontinuous lobes at depth. In Pond 2 (sandy loam), more efficient percolation and lateral spreading are implied beneath the basin, consistent with higher pore connectivity; the presence of liquid at the surface suggests active input,

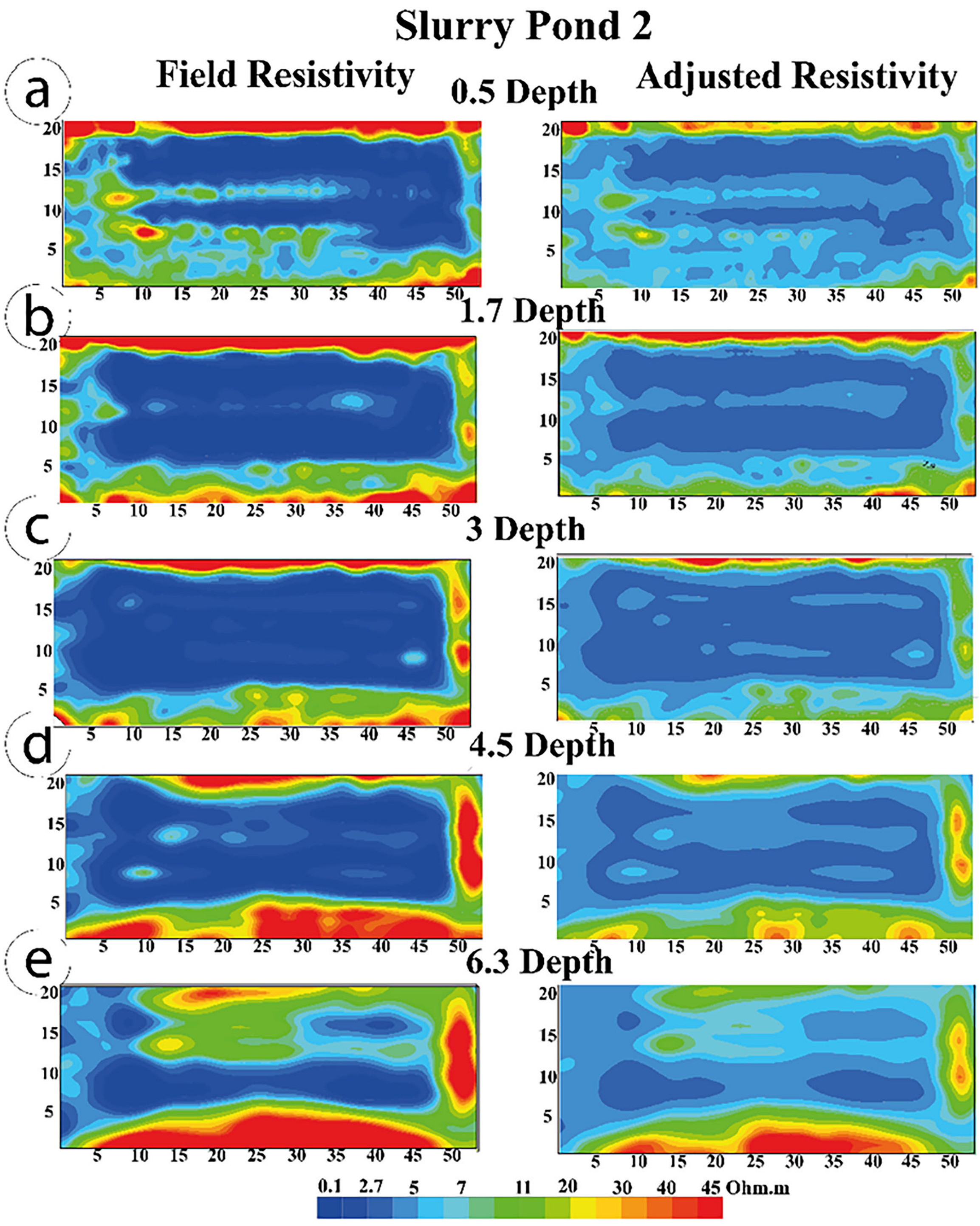

FIGURE 7 Horizontal slices for Pond 2: (left) unadjusted inverted resistivity; (right) Archie-calibrated resistivity sections. Depths: (a) 0.5 m, (b) 1.7 m, (c) 3.0 m, (d) 4.5 m, (e) 6.3 m.

whereas ponds 1 and 3, with crusted surfaces, show patterns more consistent with residual moisture.

Over time, evaporation near the surface can concentrate salts and form crusts that impede infiltration; sealing of pore throats increases resistivity and limits further percolation even if fresh slurry is added. In addition to pore-fluid conductivity changes and salt precipitation, low-resistivity anomalies may arise from conductive particles adhering to grains after slurry application. Fields et al. (2022) reported similar effects, with metal-rich solids persisting in upper layers and providing surface-conduction pathways that can mimic high water content in ERT inversions. Without field verification, mapped high-S_f zones may reflect combined effects of slurry infiltration, shallow groundwater, or spa-

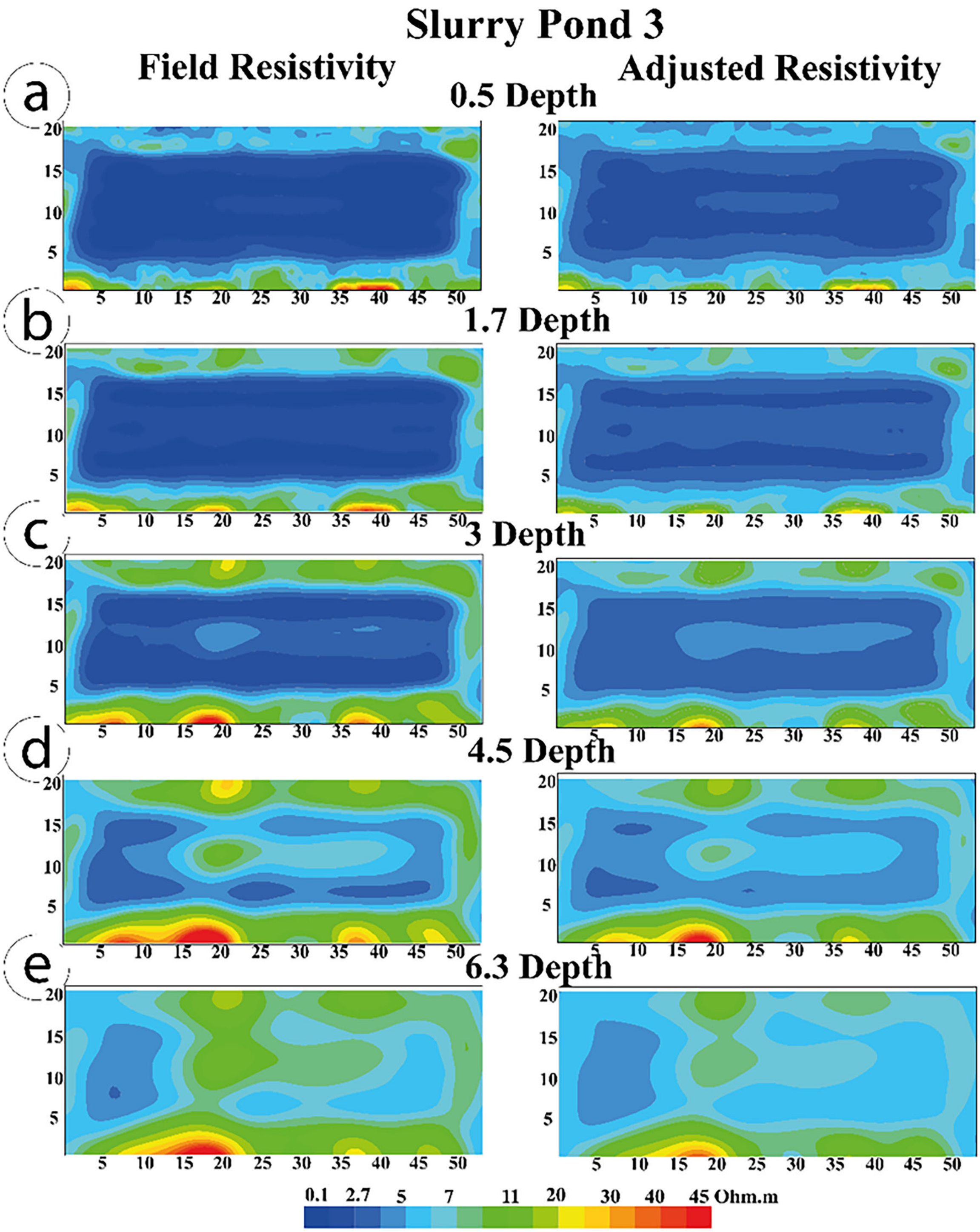

FIGURE 8 Horizontal slices for Pond 3: (left) unadjusted inverted resistivity; (right) Archie-calibrated resistivity sections. Depths: (a) 0.5 m, (b) 1.7 m, (c) 3.0 m, (d) 4.5 m, (e) 6.3 m.

tial heterogeneity in soil properties. Accordingly, these S_f maps are semi-quantitative: bulk resistivity responds to both moisture and pore-fluid conductivity, and surface-conduction changes during drying—rewetting can alter the signal. From a risk perspective, infiltration geometry has implications for groundwater protection: pond 2 (sandy loam) exhibits the highest connectivity and thus the greatest potential for deeper percolation, while pond 1 (silty clay) is more confined yet remains vulnerable to shallow leakage if the liner fails.

Operationally, the S_f maps highlight zones where liner failure or preferential pathways are most plausible. Depth extent of elevated S_f is comparable in ponds 2 and 3 (~4–5 m) and shallower in pond 1 (~3 m), while lateral spreading is greatest in pond 2. This supports targeted inspections and prioritiza-

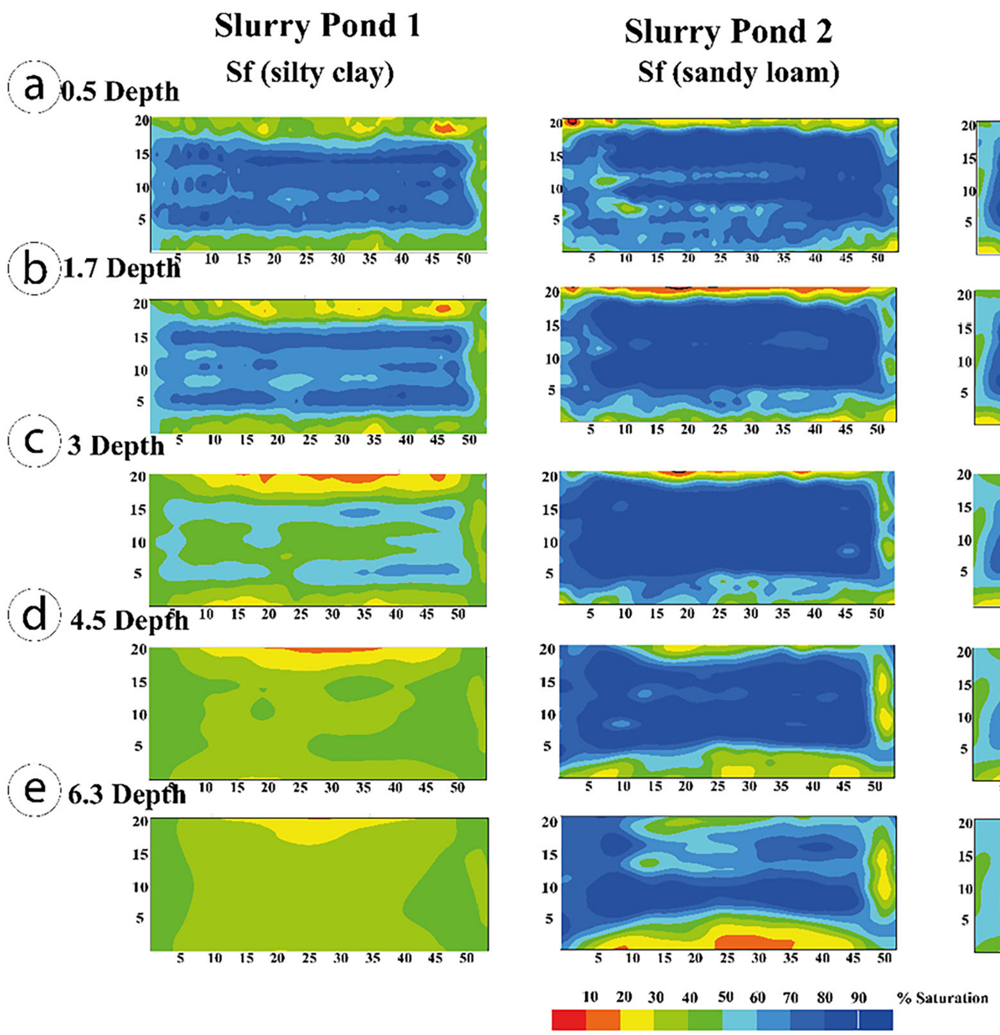

FIGURE 9 Plan-view (horizontal) slices of modified Archie-calibrated soil-slurry saturation (S_f) for the three slurry ponds. Columns correspond to ponds 1–3; rows show depths of (a) 0.5 m, (b) 1.7 m, (c) 3.0 m, (d) 4.5 m, and (e) 6.3 m below ground surface. Blue hues denote high saturation (≥80%), green–yellow moderate (30%–70%), and red low (≤20%). Spatial patterns highlight deeper, basin-wide infiltration in the sandy loam (pond 2) and shallower, more confined plumes in the finer-textured ponds 1 and 3.

tion of monitoring wells downgradient of the deepest plumes. Future work should include in-situ moisture sensing, piezometry, and chemical analyses to confirm infiltration dynamics and distinguish slurry influence from background conditions.

4 | CONCLUSIONS

By combining multi-profile ERT (2D inversions stitched into 3D volumes) with a texture-specific petrophysical calibration, semi-quantitative maps of soil slurry saturation (S_f) were produced beneath active slurry ponds. The results show a textural control on infiltration depth and geometry: deepest and laterally more extensive in the sandy loam (pond 2), intermediate in the silt loam (pond 3), and shallowest in the silty clay (pond 1). This laboratory-to-field translation enables non-destructive localization of likely leakage pathways and prioritization of targeted verification at low cost and with minimal disturbance. Because bulk resistivity is governed by both saturation and pore-fluid conductivity and given that m was selected per pond within literature bounds and ρ_f was assumed stable during the surveys, the S_f maps are semi-quantitative and should be corroborated with hydrologic and chemical measurements. This study is an initial step toward constraining Archie parameters for Mediterranean slurry-affected soils; broader texture- and site-specific calibrations are needed beyond the three soil types evaluated here.

These calibrations enabled semi-quantitative estimates of subsurface soil slurry saturation (S_f) and delineation of zones potentially affected by slurry infiltration: (i) pond 1 (silty clay): infiltration is confined to the upper ≈3 m, reflecting high water retention and low permeability; (ii) pond 2 (sandy loam): greater pore connectivity allows S_f to remain above the 48% threshold down to ∼4.5 m; and (iii) pond 3 (silt loam): S_f exceeds the 28% threshold to ∼5 m, consistent with intermediate retention and episodic ponding. These results suggest that soil texture governs both the depth and lateral extent of slurry migration. The laboratory-derived thresholds (S_f = 0.37 for silty clay, 0.48 for sandy loam, and 0.28 for silt loam) are operational markers of the regime change observed in the laboratory ρ– S_f relationship, where resistivity increases non-linearly as pore-fluid connectivity decreases (Sections 2.6 and 3.2). In the field, these thresholds support depth-based interpretation of calibrated sections by indicating where the influence of connected slurry-filled porosity likely diminishes, while recognizing that S_f estimates remain semi-quantitative.

Modified Archie's law incorporating these factors has been proposed to improve calibration accuracy, particularly in slurry-affected clayey soils. Applying texture-dependent saturation limits can help inform slurry reapplication timing, enhancing agronomic use while minimizing groundwater contamination. While the S_f maps offer a practical monitoring tool, it is important to note that they are semi-quantitative model-based estimates calibrated from gravimetric moisture-resistivity curves and not direct measurements. Their accuracy depends on laboratory-derived Archie parameters and assumptions of stable pore-fluid conductivity. In this context, high-resistivity zones observed beyond pond boundaries (typically above 18 Ω.m) combined with their spatial separation from visible infiltration plumes and location outside slurry application zones are interpreted as areas reflecting background moisture conditions unrelated to pond leakage. Future work should incorporate in situ dielectric probes and solute measurements to resolve this ambiguity.

AUTHOR CONTRIBUTIONS

Ximena Capa-Camacho: Conceptualization; formal analysis; investigation; methodology; writing—original draft. **Pedro Martínez-Pagán**: Data curation; writing—review and editing. **Ángel Faz**: Supervision; validation. **Marco Vásconez-Maza**: Supervision; validation; writing—review and editing. **Marcos A. Martínez-Segura**: Methodology. **Khadidja Delimi**: Investigation. **Oussama Jabrane**: Formal analysis; validation.

ACKNOWLEDGMENTS

This work was supported by the research grant 21583/FPI/21. Fundación Séneca. Región de Murcia (Spain).

CONFLICT OF INTEREST STATEMENT

The authors declare no conflicts of interest.

ORCID

Ximena Capa-Camacho https://orcid.org/0000-0002-0704-3359
Pedro Martínez-Pagán https://orcid.org/0000-0002-3308-3768
Ángel Faz https://orcid.org/0000-0002-9271-9818
Marco Vásconez-Maza https://orcid.org/0000-0002-6190-1027
Marcos A. Martínez-Segura https://orcid.org/0000-0002-1163-8427
Khadidja Delimi https://orcid.org/0009-0002-2599-4956
Oussama Jabrane https://orcid.org/0000-0002-6420-8017

REFERENCES

Abu-Hassanein, Z. S., Benson, C. H., & Blotz, L. R. (1996). Electrical resistivity of compacted clays. *Journal of Geotechnical Engineering*, *122*(5), 397–406.

Alam, M. M., Shaik, A. K., & Fabricius, I. L. (2010). Excess conductivity of north Sea Chalk and its influence on cementation exponent and saturation prediction. In *72nd EAGE Conference and Exhibition incorporating SPE EUROPEC 2010* (pp. cp–161). European Association of Geoscientists & Engineers. https://doi.org/10.3997/2214-4609.201400893

Andrades, M. (1996). *Prácticas de edafología y climatología*. Universidad de la Rioja.

Araya Vargas, J., Gil, P. M., Meza, F. J., Yáñez, G., Menanno, G., García-Gutiérrez, V., Luque, A. J., Poblete, F., Figueroa, R., Maringue, J., Pérez-Estay, N., & Sanhueza, J. (2020). Soil electrical resistivity monitoring as a practical tool for evaluating irrigation systems efficiency at the orchard scale: A case study in a vineyard in Central Chile. *Irrigation Science*, *39*(1), 123–143. https://doi.org/10.1007/S00271-020-00708-W

Arbat, G., Roselló, A., Domingo Olivé, F., Puig-Bargués, J., González Llinàs, E., Duran-Ros, M., Pujol, J., & Ramírez de Cartagena, F. (2013). Soil water and nitrate distribution under drip irrigated corn receiving pig slurry. *Agricultural Water Management*, *120*, 11–22. https://doi.org/10.1016/j.agwat.2012.08.001

Archie, G. E. (1942). The electrical resistivity log as an aid in determining some reservoir characteristics. *Transactions of the AIME*, *146*(1), 54–62. https://doi.org/10.2118/942054-G

Baxter, S. (2007). World Reference Base for Soil Resources. World Soil Resources Report 103. Rome: Food and Agriculture Organization of the United Nations (2006), pp. 132, ISBN 92-5-10511-4. *Experimental Agriculture*, *43*(2), 264–264. https://doi.org/10.1017/S0014479706394902

Bernal, M. P., Roig, A., Lax, A., & Navarro, A. F. (1992). Effects of the application of pig slurry on some physico-chemical and physical properties of calcareous soils. *Bioresource Technology*, *42*(3), 233–239. https://doi.org/10.1016/0960-8524(92)90026-T

Bernal, M. P., Roig, A., Madrid, R., & Navarro, A. F. (1992). Salinity risks on calcareous soils following pig slurry applications. *Soil Use and Management*, *8*(3), 125–129.

Binley, A., & Kemna, A. (2005). DC resistivity and induced polarization methods. In Y. Rubin & S. S. Hubbard (Eds.), *Hydrogeophysics* (pp. 129–156). Springer. https://doi.org/10.1007/1-4020-3102-5_5

Boitt, G., Marchezan, C., Ceretta, C. A., Brunetto, G., Lourenzi, C. R., Girotto, E., Ferreira, P. A. A., Basso, C. J., Gatiboni, L. C., & Condron, L. (2022). The fate of pig slurry phosphorus applied to a sandy loam soil under no-till cropping in southern Brazil. *Geoderma*, *422*, 115931. https://doi.org/10.1016/j.geoderma.2022.115931

Bonmatí, A., Campos, E., & Flotats, X. (2003). Concentration of pig slurry by evaporation: Anaerobic digestion as the key process. *Water Science and Technology*, *48*(4), 189–194. https://doi.org/10.2166/wst.2003.0252

Capa-Camacho, X., Martínez-Pagán, P., Acosta, J. A., Martínez-Segura, M. A., Vásconez-Maza, M., & Faz, Á. (2024). Environmental monitoring of pig slurry ponds using geochemical and geoelectrical techniques. *Water*, *16*(7), 1016. https://doi.org/10.3390/w16071016

Ceretta, C. A., Girotto, E., Lourenzi, C. R., Trentin, G., Vieira, R. C. B., & Brunetto, G. (2010). Nutrient transfer by runoff under no tillage in a soil treated with successive applications of pig slurry. *Agriculture, Ecosystems and Environment*, *139*(4), 689–699. https://doi.org/10.1016/j.agee.2010.10.016

Chambers, J. E., Kuras, O., Meldrum, P. I., Ogilvy, R. D., & Hollands, J. (2006). Electrical resistivity tomography applied to geologic, hydrogeologic, and engineering investigations at a former waste-disposal site. *Geophysics*, *71*(6), B231–B239. https://doi.org/10.1190/1.2360184

Choo, H., Park, J., Do, T. T., & Lee, C. (2022). Estimating the electrical conductivity of clayey soils with varying mineralogy using the index properties of soils. *Applied Clay Science*, *217*, 106388. https://doi.org/10.1016/j.clay.2021.106388

Corwin, D. L., & Lesch, S. M. (2013). Protocols and guidelines for field-scale measurement of soil salinity distribution with EC a -directed soil sampling. *Journal of Environmental and Engineering Geophysics*, *18*(1), 1–25. https://doi.org/10.2113/JEEG18.1.1

Dahlin, T., & Zhou, B. (2004). A numerical comparison of 2D resistivity imaging with 10 electrode arrays. *Geophysical Prospecting*, *52*(5), 379–398. https://doi.org/10.1111/j.1365-2478.2004.00423.x

de Rosa Couto, R., Santos, M. D., Comin, J. J., Pittol Martini, L. C., Gatiboni, L. C., Martins, S. R., Filho, P. B., & Brunetto, G. (2015). Environmental vulnerability and phosphorus fractions of areas with pig slurry applied to the soil. *Journal of Environmental Quality*, *44*(1), 162–173. https://doi.org/10.2134/jeq2014.08.0359

Datsios, Z. G., Mikropoulos, P. N., & Karakousis, I. (2017). Laboratory characterization and modeling of DC electrical resistivity of sandy soil with variable water resistivity and content. *IEEE Transactions on Dielectrics and Electrical Insulation*, *24*(5), 3063–3072. https://doi.org/10.1109/TDEI.2017.006583

de Cássia Goulart Ferreira, Q., de Almeida Prado Bacellar, L., & Moreira Viana, J. H. (2021). Evaluation of soil moisture by electrical resistivity in oxisols of the central Brazilian savanna. *Geoderma Regional*, *26*, e00408. https://doi.org/10.1016/j.geodrs.2021.e00408

Díez, J. A., Hernaiz, P., Muñoz, M. J., de la Torre, A., & Vallejo, A. (2006). Impact of pig slurry on soil properties, water salinization, nitrate leaching and crop yield in a four-year experiment in Central Spain. *Soil Use and Management*, *20*(4), 444–450. https://doi.org/10.1111/j.1475-2743.2004.tb00395.x

Du, L., Han, Y., Wang, Y., Hu, X., Yao, R., & Zhang, X. (2021). Calculation of cementation factor and saturation exponent by resistivity: A case study of silty clay formation, Changchun, China. *Arabian Journal of Geosciences*, *14*(18), 1833. https://doi.org/10.1007/s12517-021-08199-5

Escosa, F. O., Ferrer, O., & Roca, E. (2018). Geology of the Eastern Prebetic Zone at the Jumilla region (SE Iberia). *Journal of Maps*, *14*(2), 77–86. https://doi.org/10.1080/17445647.2018.1433562

FAO. (2006). *Guidelines for soil description*. https://library.wur.nl/WebQuery/wurpubs/355777

Fields, J., Halihan, T., Vilcaez, J., Sharpley, A. N., & Daniels, M. (2022). Hydrogeophysical characterization of swine effluent amended soils in mantled karst. *Journal of the ASABE*, *65*(6), 1317–1332. https://doi.org/10.13031/JA.15259

Fu, Y., Horton, R., Ren, T., & Heitman, J. L. (2021). A general form of Archie's model for estimating bulk soil electrical conductivity. *Journal of Hydrology*, *597*, 126160. https://doi.org/10.1016/j.jhydrol.2021.126160

García, C. C., & Sarria, F. A. (2006). El clima de la Región de Murcia. In *El medio físico de la Región de Murcia* (pp. 95–128). Universidad de Murcia.

Glover, P. W. J. (2016). Archie's law—A reappraisal. *Solid Earth*, *7*(4), 1157–1169. https://doi.org/10.5194/se-7-1157-2016

Hashemi, S. A., Spelay, R. B., Sanders, R. S., & Hjertaker, B. T. (2021). A novel method to improve electrical resistance tomography measurements on slurries containing clays. *Flow Measurement and Instrumentation*, *80*, 101973. https://doi.org/10.1016/j.flowmeasinst.2021.101973

Hayley, K., Bentley, L. R., & Pidlisecky, A. (2010). Compensating for temperature variations in time-lapse electrical resistivity difference imaging. *Geophysics*, *75*(4), WA51–WA59. https://doi.org/10.1190/1.3478208

Helene, L. P. I., Moreira, C. A., & Bovi, R. C. (2020). Identification of leachate infiltration and its flow pathway in landfill by means of electrical resistivity tomography (ERT). *Environmental Monitoring and Assessment*, *192*(4), 249. https://doi.org/10.1007/s10661-020-8206-5

Holmes, J., Chambers, J., Wilkinson, P., Dashwood, B., Gunn, D., Cimpoiaşu, M., Kirkham, M., Uhlemann, S., Meldrum, P., Kuras, O., Huntley, D., Abbott, S., Sivakumar, V., & Donohue, S. (2022). 4D electrical resistivity tomography for assessing the influence of vegetation and subsurface moisture on railway cutting condition. *Engineering Geology*, *307*(March), 106790. https://doi.org/10.1016/j.enggeo.2022.106790

Horváth, A., Makó, A., Bidló, A., & Szecsődi, O. (2021). *Estimation of water holding capacity of soils using data from different types of particle size analyses*. https://doi.org/10.5194/egusphere-egu21-12921

IGME. (1993). *Mapa Geológio de España. Escala 1:200 000*. Fuente Álamo—Murcia.

Innocenti, A., Pazzi, V., Napoli, M., Fanti, R., & Orlandini, S. (2024). Assessing the efficiency of the irrigation system in a horticulture field through time-lapse electrical resistivity tomography. *Irrigation Science*, *43*(6), 1437–1451. https://doi.org/10.1007/S00271-024-00919-5

IUSS Working Group WRB. (2022). World reference base for soil resources. International soil classification system for naming soils and creating legends for soil maps. *Journal of Plant Nutrition and Soil Science*, *186*(2), 151–163. https://doi.org/10.1002/jpln.202200417

Jardé, E., Gruau, G., Mansuy-Huault, L., Peu, P., & Martinez, J. (2007). Using sterols to detect pig slurry contribution to soil organic matter. *Water, Air, & Soil Pollution*, *178*(1–4), 169–178. https://doi.org/10.1007/s11270-006-9188-9

Kazemzadeh, E., Nabi-Bidhendi, M., Moezabad, M. K., Rezaee, M. R., & Saadat, K. (2007). A new approach for the determination of cementation exponent in different petrofacies with velocity deviation logs and petrographical studies in the carbonate Asmari formation. *Journal of Geophysics and Engineering*, *4*(2), 160–170. https://doi.org/10.1088/1742-2132/4/2/005

Kelly, B. F. J., Acworth, R. I., & Greve, A. K. (2011). Better placement of soil moisture point measurements guided by 2D resistivity tomography for improved irrigation scheduling. *Soil Research*, *49*(6), 504–512. https://doi.org/10.1071/SR11145

Kuras, O., Wilkinson, P. B., Meldrum, P. I., Oxby, L. S., Uhlemann, S., Chambers, J. E., Binley, A., Graham, J., Smith, N. T., & Atherton, N. (2016). Geoelectrical monitoring of simulated subsurface leakage to support high-hazard nuclear decommissioning at the Sellafield Site, UK. *Science of the Total Environment*, *566–567*, 350–359. https://doi.org/10.1016/j.scitotenv.2016.04.212

Liu, S., Chen, L., & Han, L. (2008). Study on electrical resistivity related parameters of contaminated soils. In *Geotechnical engineering for disaster mitigation and rehabilitation: Proceedings of the 2nd International Conference GEDMAR08* (pp. 695–701). Springer Berlin Heidelberg. https://doi.org/10.1007/978-3-540-79846-0

Loke, M. H., & Barker, R. D. (1996). Rapid least-squares inversion of apparent resistivity pseudosections by a quasi-Newton method. *Geophysical Prospecting*, *44*(1), 131–152. https://doi.org/10.1111/j.1365-2478.1996.tb00142.x

López Bermúdez, F., Conesa García, C., Alonso Sarria, F., & Belmonte Serrato, F. (2013). La cuenca experimental de Rambla Salada (Murcia) : Investigaciones hidrogeomorfológicas. *Cuadernos de Investigación Geográfica*, *26*, 95–112. https://doi.org/10.18172/cig.1065

Maes, D. G. D., Dewulf, J., Piñeiro, C., Edwards, S., & Kyriazakis, I. (2020). A critical reflection on intensive pork production with an emphasis on animal health and welfare. *Journal of Animal Science*, *98*, S15–S26. https://doi.org/10.1093/jas/skz362

Mallmann, F. J. K., Dos Santos, D. R., Ceretta, C. A., Cella, C., Šimůnek, J., & Van Oort, F. (2012). Modeling field-scale vertical movement of zinc and copper in a pig slurry-amended soil in Brazil. *Journal of Hazardous Materials*, *243*, 223–231. https://doi.org/10.1016/j.jhazmat.2012.10.022

Margalef-Marti, R., Llovet, A., Carrey, R., Ribas, A., Domene, X., Mattana, S., Chin-Pampillo, J., Mondini, C., Alcañiz, J. M., Soler, A., & Otero, N. (2021). Impact of fertilization with pig slurry on the isotopic composition of nitrate retained in soil and leached to groundwater in agricultural areas. *Applied Geochemistry*, *125*, 104832. https://doi.org/10.1016/j.apgeochem.2020.104832

Margesin, R., & Schinner, F. (2005). *Monitoring and assessing soil bioremediation*. Springer. https://doi.org/10.1007/3-540-28904-6

Marszałek, M., Kowalski, Z., & Makara, A. (2019). The possibility of contamination of water-soil environment as a result of the use of pig slurry. *Ecological Chemistry and Engineering S*, *26*(2), 313–330. https://doi.org/10.1515/eces-2019-0022

Martínez-Pagán, P., Cano, Á. F., Ramos Da Silva, G. R., & Olivares, A. B. (2010). 2-D electrical resistivity imaging to assess slurry pond subsoil pollution in the southeastern region of Murcia, Spain. *Journal of Environmental and Engineering Geophysics*, *15*(1), 29–47. https://doi.org/10.2113/JEEG15.1.29

Merritt, A. J., Chambers, J. E., Wilkinson, P. B., West, L. J., Murphy, W., Gunn, D., & Uhlemann, S. (2016). Measurement and modelling of moisture-electrical resistivity relationship of fine-grained unsaturated soils and electrical anisotropy. *Journal of Applied Geophysics*, *124*, 155–165. https://doi.org/10.1016/j.jappgeo.2015.11.005

Oh, T.-M., Cho, G.-C., & Lee, C. (2014). Effect of soil mineralogy and pore-water chemistry on the electrical resistivity of saturated soils. *Journal of Geotechnical and Geoenvironmental Engineering*, *140*(11), 06014012. https://doi.org/10.1061/(ASCE)GT.1943-5606.0001175

Otabbong, E., Arkhipchenko, I., Orlova, O., Barbolina, I., & Shubaeva, M. (2007). Impact of piggery slurry lagoon on the environment: A study of groundwater and river Igolinka at the Vostochnii Pig Farm, St. Petersburg, Russia. *Acta Agriculturae Scandinavica Section B: Soil and Plant Science*, *57*(1), 74–81. https://doi.org/10.1080/09064710600933228

Revil, A., Cathles, L. M., Losh, S., & Nunn, J. A. (1998). Electrical conductivity in shaly sands with geophysical applications. *Journal of Geophysical Research: Solid Earth*, *103*(10), 23925–23936. https://doi.org/10.1029/98jb02125

Reynolds, J. M. (1997). *An introduction to applied and environmental geophysics*.Wiley.

Schwartz, B. F., Schreiber, M. E., & Yan, T. (2008). Quantifying field-scale soil moisture using electrical resistivity imaging. *Journal of Hydrology*, *362*(3–4), 234–246. https://doi.org/10.1016/j.jhydrol.2008.08.027

Telford, W. M., Geldart, L. P., & Sheriff, R. E. (1990). *Applied geophysics*. Cambridge University Press. https://books.google.com/books/about/Applied_Geophysics.html?hl=es&id=oRP5fZYjhXMC

Tiab, D., & Donaldson, E. C. (2003). *Petrophysics: Theory and practice of measuring reservoir rock and fluid transport properties*. Gulf Professional Pubication/Elsevier. https://doi.org/10.1016/B978-0-7506-7711-0.X5000-2

Tóth, E., Dencső, M., Horel, Á., Pirkó, B., & Bakacsi, Z. (2022). Influence of pig slurry application techniques on soil CO_2, N_2O, and NH_3 emissions. *Sustainability*, *14*(17), 11107. https://doi.org/10.3390/su141711107

Tso, C. H. M., Kuras, O., Wilkinson, P. B., Uhlemann, S., Chambers, J. E., Meldrum, P. I., Graham, J., Sherlock, E. F., & Binley, A. (2017). Improved characterisation and modelling of measurement errors in electrical resistivity tomography (ERT) surveys. *Journal of Applied Geophysics*, *146*, 103–119. https://doi.org/10.1016/j.jappgeo.2017.09.009

United Nations. (2015). THE 17 GOALS. Sustainable development. In Department of Economic and Social Affairs | Sustainable Development. https://sdgs.un.org/goals

How to cite this article: Capa-Camacho, X., Martínez-Pagán, P., Faz, Á., Vásconez-Maza, M., Martínez-Segura, M. A., Delimi, K., & Jabrane, O. (2026). Assessment of soil slurry saturation and slurry infiltration in pig slurry storage ponds using electrical resistivity tomography. *Vadose Zone Journal*, *25*, e70098. https://doi.org/10.1002/vzj2.70098